Inorganic Chemistry
Cite This: Inorg. Chem. XXXX, XXX, XXX–XXX
Article
pubs.acs.org/IC

Ruthenium-Chelated Non-Innocent Bis(heterocyclo)methanides: A Mimicked β-Diketiminate

Sanjib Panda,* Sudip Kumar Bera, Puneet Goel, Achintya Kumar Dutta, and Goutam Kumar Lahiri*

Department of Chemistry, Indian Institute of Technology Bombay, Powai, Mumbai 400076, India

Supporting Information

ABSTRACT: The unexplored substrate-based reactivity profile of newly designed bis(heterocyclo)methanide (BHM, L1−L3), a structural mimic of ubiquitous β-diketiminate, was demonstrated on an electronically rich {Ru(acac)$_2$} platform (acac = σ-donating acetylacetonate). In this regard, this work deals with structurally characterized [Ru(L)(acac)$_2$] complexes **1A−3A** incorporating electronically varying heterocycles {**1A**, L1 = bis(imidazo[1,5-*a*]pyridin-3-yl)methanide; **2A**, L2 = (*Z*)-4-[(6,7-dihydrothieno[3,2-*c*]pyridin-4-yl)methylene]-6,7-dihydro-4*H*-thieno[3,2-*c*]pyridin-5-ide; **3A**, L3 = (*Z*)-6-chloro-1-[(6-chloro-3,4-dihydroisoquinolin-1-yl)methylene]-3,4-dihydro-1*H*-isoquinolin-2-ide}. The significant impact of electronic modification at the BHM backbone (L1−L3) on its redox tunability at the metal−ligand interface in **1A−3A** and its subsequent oxygenation profile to yield bis(heterocyclo)methanone (BMO, analogue of α-ketodiimine) in the corresponding [Ru(BMO)(acac)$_2$] (**1B−3B**) via a radical pathway were rationalized. In addition, oxidative dehydrogenation of metalated BMO in **1B−3B** to BAM [bis(heteroaryl)methanone] in [Ru(BAM))-(acac)$_2$] (**1C−3C**) was illustrated in support of the nonspectator behavior of α-ketodiimine. A combined experimental and theoretical investigation extended mechanistic outlines of the aforementioned transformation processes, which in effect provided a new dimension relating to the analogous β-diketiminate as well as α-ketodiimine chemistry.

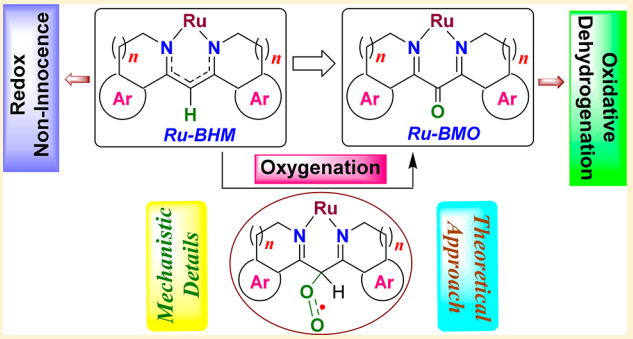

INTRODUCTION

Conversion of earth-abundant and readily accessible small molecules such as O_2, N_2, H_2, CO_2, CH_4, etc., into value-added chemical feedstock under mild reaction conditions has been considered to be an important event in terms of industry and the environment.[1] However, chemical transformations of these molecules are thermodynamically demanding and mechanistically complex owing to the inertness of their bonds, and their activation poses a formidable challenge. In fact, redox active ligand-derived metal complex-mediated small molecule activation as well as functionalization of inert bonds has garnered significant attention for the introduction of structural diversity into the substrate backbone.[1c−h]

In this context, application of the β-diketiminate (nacnac) moiety in small molecule activation has been well documented primarily due to its stereoelectronic tunability.[2] In addition to its robust nature, the nonspectator feature of nacnac has also led to ligand-based reactivity involving its nucleophilic methine carbon (C_β).[3−5] In addition, establishment of the hidden redox non-innocence of nacnac due to its odd number of p orbitals in the π-system is a challenging task, though a few reports have emphasized this.[6] However, recent efforts have been devoted to the design of a variety of bis(heterocyclo)methanides (BHM) comprising of a nacnac core with substitution at the extended π-conjugated ring to modulate its steric and electronic demands.[7] Furthermore, in lieu of methyl substituents at the C_α position of nacnac, the aryl group of BHM prevents deprotonation to inhibit unwanted acid/base chemistry.[8] In this regard, this study highlights the reactivity profile of rarely explored BHM derivatives via O_2 activation in the vein of nacnac chemistry.

Thus, the redox behavior of the newly designed BHM derivatives (L1−L3) has been invoked to rationalize the oxygenation of BHM to BMO [bis(heterocyclo)methanone] upon coordination with the electronically rich {Ru(acac)$_2$} (acac = acetylacetonate) metal fragment (Figure 1). The kinetic instability of the complexes has been addressed by varying the aryl substituents of the BHM moiety.

Structural and mechanistic details along with the correlation of reactivity have been authenticated by spectroscopic and theoretical details. To the best of our knowledge, this work demonstrates for the first time the activation of a small molecule at the backbone of BHM. On the other hand, oxidative dehydrogenation of BMO to bis(heteroaryl)-methanone (BAM) (Figure 1) implies its chemical non-innocence, as well. It is worth noting that metal coordination-assisted oxidative dehydrogenation of the C−C bond is a widely applicable strategy for generating nitrogen heteroarenes from their corresponding heterocyclic counterparts.[9]

Received: April 24, 2019

DOI: 10.1021/acs.inorgchem.9b01201
Inorg. Chem. XXXX, XXX, XXX−XXX

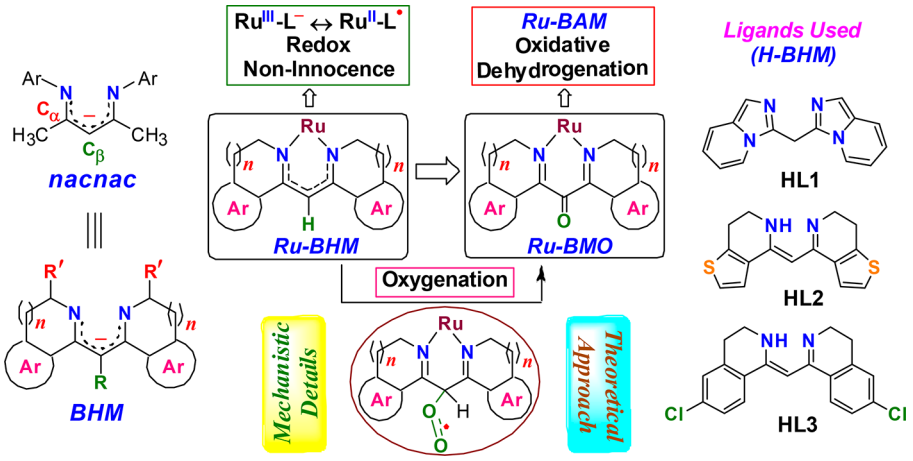

Figure 1. Ru chelation-assisted transformations of BHM and BMO.

Scheme 1. Synthetic Aspects of H-BHM[a]

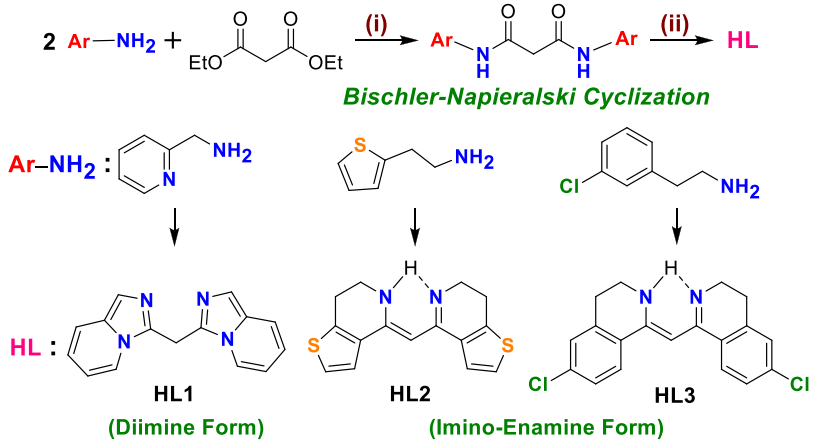

[a]Conditions: (i) reflux, 48 h; (ii) P_2O_5, $POCl_3$, toluene, reflux, 12 h.

RESULTS AND DISCUSSION

Synthetic and Structural Aspects. The homodisubstituted H-BHM ligands (**HL1**−**HL3**) were obtained by following the Bischler−Napieralski reaction pathway,[10] starting from the condensation of diethylmalonate and corresponding amines followed by acid-promoted cyclization of the preformed malonamide (Scheme 1). The *para* selectivity in **HL3** due to the diminished electron density at the adjacent *ortho* position of the chloro substituent could be attributed to the calculation of Fukui indices (Figure S1).[11] Ligands are expected to exist in either the diimine or the iminoenamine tautomeric form as a consequence of mesomeric stabilization.[12] However, bis(imidazopyridin-3-yl)methane (**HL1**) stabilizes in the diimine form due to the formation of an aromatic 10π-heterocyclic system [each imidazopyridine ring follows (4n + 2)π bridged by the methylene group]. On the other hand, the preferential hydrogen-bonded iminoenamine form for **HL2** or **HL3** is reflected in its nuclear magnetic resonance (NMR) profiles and structural parameters (see below and the Supporting Information).

$\{Ru^{III}(acac)_2\}$-bonded BHMs (**1A**−**3A**) were obtained from H-BHM and $[Ru^{II}(acac)_2(CH_3CN)_2]$ (Scheme 2). Like nacnac, deprotonated BHM coordinates to the metal ion through its imine nitrogen donors, forming a six-membered metallaheterocycle. The initially formed complexes, **1A**−**3A**, are however sensitive to air and undergo irreversible transformation to the corresponding metalated BMO [BMO = bis(heterocyclo)methanone] species in **1B**−**3B** under ambient conditions, where insertion of oxygen into the C(sp^2)−H bond of monoanionic BHM in **A** results in a new C═O bond in **B** (neutral ketodiimine) with the simultaneous reduction of the metal oxidation state from Ru(III) to Ru(II).

The change in bond parameters, diamagnetic $^1H/^{13}C$ NMR signals, the disappearance of electron paramagnetic resonance (EPR) signatures, characteristic electronic spectra, and varying redox potentials upon moving from **A** to **B** (see below) collectively corroborate the reduction in the reaction sequence from **A** to **B**. The rate of conversion of **A** to **B** varies on the basis of the nature of the C_α-substituted side arm and decreases in the order **1A** ≫ **2A**. On the contrary, oxygenation of **3A** to **3B** is too slow to follow kinetically, which in turn facilitates for the production of the single crystal of **3A**. The involvement of aerial oxygen for **A** → **B** conversion has been established by an $^{18}O_2$ labeling experiment with the representative complex **1A** (Figure S2b). Subsequently, **2B** or **3B** undergoes aerobic dehydrogenation of the N(imine)-substituted methylene centers of pro-aromatic BMO to yield fully aromatic BAM [BAM = bis(heteroaryl)methanone] in **2C** or **3C**, respectively. The rate of **B** → **C** conversion is however

DOI: 10.1021/acs.inorgchem.9b01201
Inorg. Chem. XXXX, XXX, XXX−XXX

Scheme 2. Synthetic Outline for A–C[a]

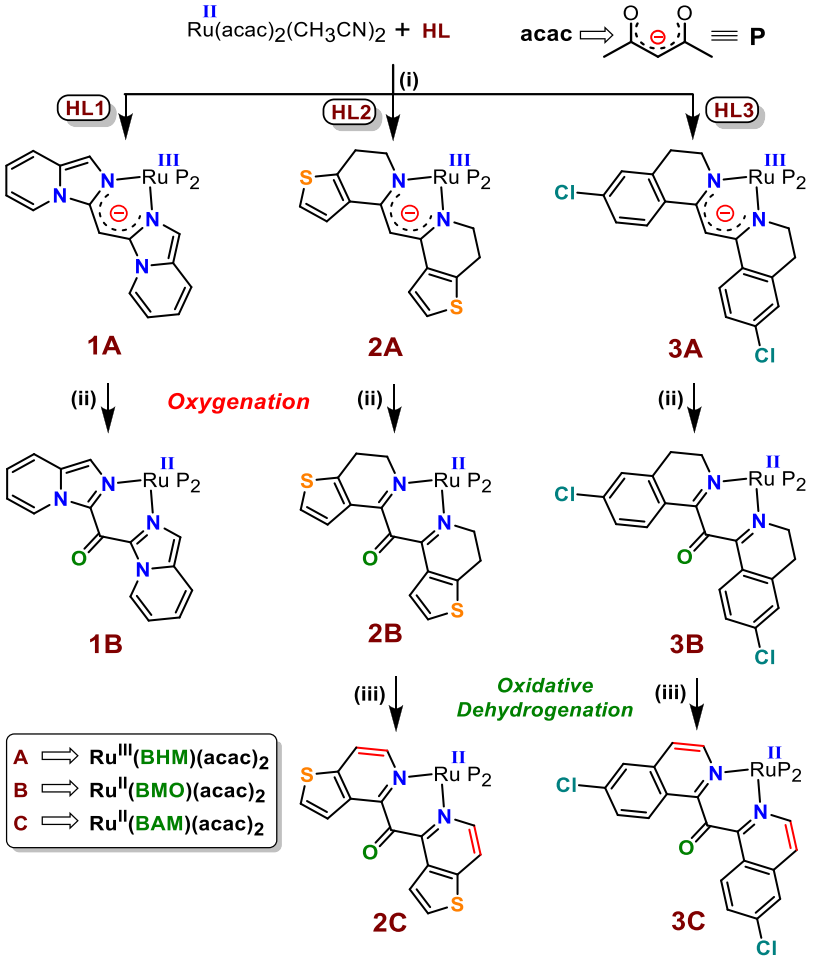

[a]Conditions: (i) EtOH, Et_3N, 373 K, ~4 h; (ii and iii) EtOH, O_2 balloon, 373 K.

found to be much faster in the presence of a base such as Et_3N or ^tBuOK.

The identities of the complexes have been authenticated by their single-crystal X-ray structures, ESI-MS, and spectroscopic [$^1H/^{13}C$ NMR, EPR, ultraviolet–visible–near infrared (UV–vis–NIR), and infrared (IR)] and electrochemical signatures.

Crystal structures of representative **3A**, **1B**, **2B**, **2C**, **HL3**, and **3C** are shown in Figure 2 and Figures S3–S5. Crystallographic and bond parameters are listed in Table 1 and Tables S1–S6, respectively. The two independent molecules in the asymmetric unit of **3A** or **3C** exhibited similar bond parameters.

Complexes form a distorted octahedral geometry around the central Ru ion with *trans* and *cis* angles of 176–179° and 85–96°, respectively. N1–C1 [1.338(10) Å] and C1–C2 [1.409(11) Å] bond lengths (Table 1) of **3A** support delocalization of the negative charge in the BHM (L3) backbone, while the N1–C1 bond length of 1.302(5) Å in **2B** is in agreement with its double bond character. The relatively longer N1–C1 bond distance in **1B** or **2C** can be attributed to the aromatic ring character/electronic feature of the metalated ligand backbone along with a greater extent of $Ru^{II}(d\pi) \rightarrow L(\pi^*)$ back-donation[13] in the bonding synergism. It has also been reflected in the slightly elongated C=O bond in **1B** or **2C** in comparison to the unperturbed C=O bond in **2B** (Table 1). The shifting of the C=O stretching frequency (Experimental Section) toward the higher-energy region upon moving from **1B** to **2B** to **3B** also suggests the varying electronic nature of the ligand backbone as well as back-donation. Moreover, back-donation causes red shifting of the lowest-energy band (~200 nm) upon moving from **A** to **B** (see below). The planarity of isoquinoline units in **2C** along with the shortening of C8–C9/C4–C5 bonds and the disappearance of the ^1H NMR signature of methylene protons upon moving from **2B** to **2C** are consistent with the $CH_2 \rightarrow CH$ conversion in the reaction sequence. The partial double bond character of the C1–C2 [1.423(5) Å] and N1–C1 [1.319(5) Å] bonds of **HL3** (Figure S3 and Table S3) is also authenticated by its iminoenamine tautomeric form.

Spectral, Electrochemical, and Electronic Structural Aspects. The identities of **HL1–HL3** ligands and diamagnetic complexes **B**/**C** have been authenticated by their $^1H/^{13}C$/DEPT-135 NMR signatures (Figure S6). The absence of the NH signal as well as the appearance of a sharp peak corresponding to two protons (methylene CH_2) at δ = 4.78 ppm in the ^1H NMR spectrum and the signal at 26.98 ppm with the inverted phase in the DEPT-135 NMR spectrum corroborate the diimine form of **HL1**. On the other hand, the preferential iminoenamine form of H-bonded **HL2** or **HL3** is reflected in its broad NH ($\delta \sim$ 11.5 ppm) and sharp methine C–H ($\delta \sim$ 5.5 ppm) resonances.

DOI: 10.1021/acs.inorgchem.9b01201
Inorg. Chem. XXXX, XXX, XXX–XXX

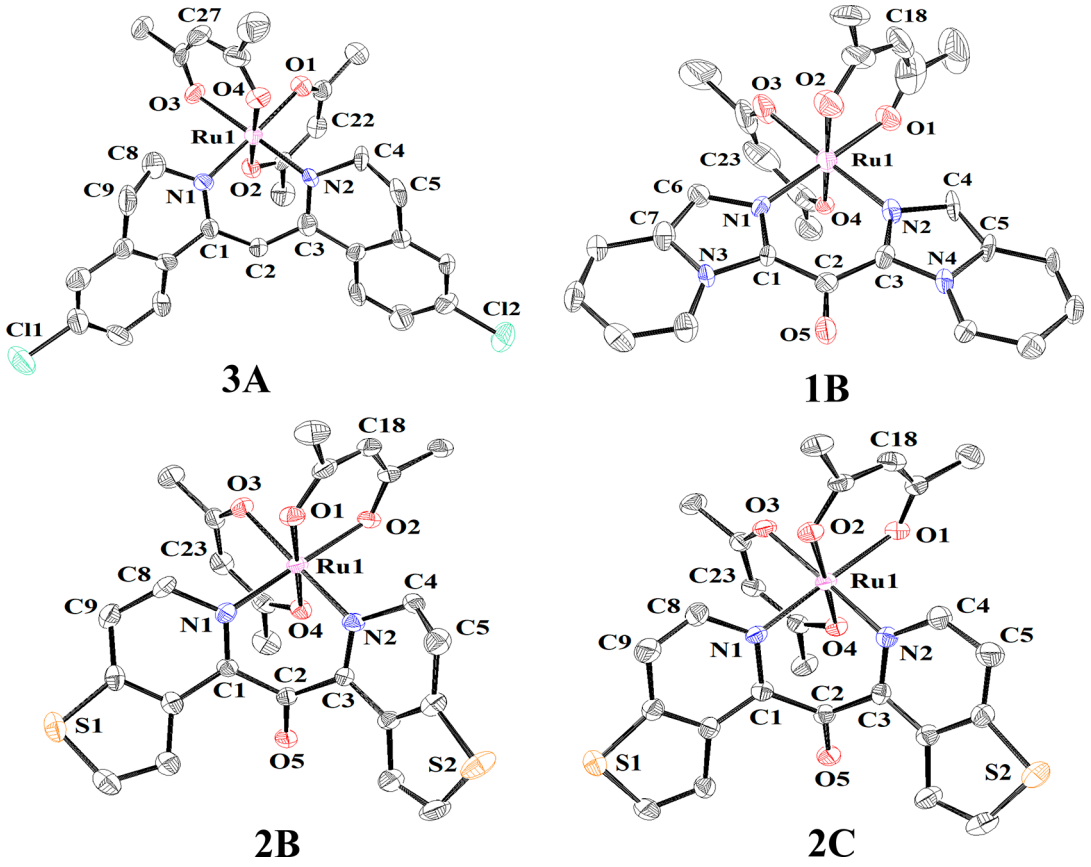

Figure 2. ORTEP diagrams of **3A** (molecule A), **1B**, **2B**, and **2C**. Hydrogen atoms and solvent molecules have been omitted for the sake of clarity. Thermal ellipsoids are at the 50% probability level.

Table 1. Selected Bond Lengths (angstroms)

	3A (molecule A)	1B	2B	2C
Ru1–N1	1.974(7)	2.015(8)	1.972(3)	1.987(4)
N1–C1	1.338(10)	1.342(11)	1.302(5)	1.353(6)
C1–C2	1.409(11)	1.451(12)	1.500(5)	1.480(7)
C2–O5	–	1.238(12)	1.224(4)	1.234(6)
C8–C9	1.477(12)	–	1.536(6)	1.365(9)

Table 2. Electronic Spectral Data of Complexes in CH_3CN

complex	λ (nm) (ε (M^{-1} cm^{-1}))
1B	400 (18200), 446 (12000), 677 (2400)
2A	275 (25200), 349 (18000), 441 (8000), 616 (1800)
2B	335 (3000), 436 (8300), 574 (3000), 816 (450)
2C	340 (5300), 430 (6500), 606 (2700), 820 (530)
3A	350 (8200), 453 (6400), 610 (1220)
3B	344 (900), 458 (1240), 651 (3100), 830 (800)
3C	340 (14720), 480 (14270), 650 (7358), 820 (1580)

The conversion of the central C–H of BHM in **A** to a C=O in **B** is supported by the disappearance of its methine proton (^{1}H NMR) as well as by the appearance of a new C=O peak in the ^{13}C NMR spectrum. Moreover, **2B** or **3B** exhibits nearby proton resonances at ~3.7 and ~2.8 ppm corresponding to methylene protons adjacent to imine nitrogens as has also been recognized by ^{13}C/DEPT NMR. However, these peaks have diaappeared upon moving from **B** to **C** with the simultaneous appearance of new peaks in the aromatic region, suggesting the increase in aromaticity.

Complexes exhibit multiple absorptions in the UV–vis–NIR region, which have been analyzed by the time-dependent density functional (TD-DFT) formalism (Table 2 and Figure S7 and Table S7). The lowest-energy absorption bands for {Ru(acac)$_2$}-coordinated BHM in **A** and BMO/BAM in **B**/**C** originate from ligand to metal (LMCT, BHM → Ru^{III}) and metal to ligand (MLCT, Ru^{II} → π^* of BMO/BAM) charge transfer transitions, respectively. The red shifting of the lowest-energy band (~200 nm) upon moving from **A** to **B** takes place due to the low-lying π^* orbital of the strongly π-accepting BMO in **B**.[13] A similar trend is also reflected in the absorption profile of **C** because of the similar π-acidic nature of BAM in **C**.

The impact of the electronic modulation of BHM (L1–L3) in paramagnetic **1A–3A** [$S = {}^1/_2$ (Scheme 2)] toward its redox non-innocence (RNI) has been defined by EPR (Figure 3 and Table S8) and the DFT-calculated spin density (SD) distribution (Figure 4 and Table S9). Primarily ligand-centered EPR for **1A** ($\Delta g = 0.015$) and metal-based anisotropic EPR for **2A** and **3A** ($\Delta g \sim 0.21$) along with their SD distribution (Ru/L) (**1A**, 0.26/0.74; **2A**, 0.68/0.28; **3A**, 0.69/0.27) suggest the dominating elctronic structural forms of Ru^{II}-L1$^{\bullet}$ and Ru^{III}-L2^{-}/Ru^{III}-L3^{-}, respectively.[14] However, partial spin accumulation on L2/L3 in **2A**/**3A** leads to the consideration of Ru^{II}-L2$^{\bullet}$/Ru^{II}-L3$^{\bullet}$ as a minor contributing resonance form. Electron pushing from the bridgehead N atoms (N3/N4) indeed favors intramolecular electron transfer (Ru^{III}-L1^{-} ↔ Ru^{II}-L1$^{\bullet}$) to give rise to the radical state of L1$^{\bullet}$ preferentially in **1A**. This in turn emphasizes the varying RNI of BHM as a function of

DOI: 10.1021/acs.inorgchem.9b01201
Inorg. Chem. XXXX, XXX, XXX–XXX

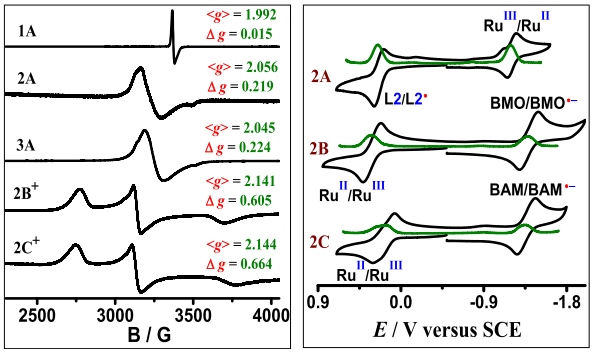

Figure 3. X-Band EPR spectra (left) at 100 K in CH_3CN-toluene. $\langle g \rangle = \{(^1/_3)(g_1^2 + g_2^2 + g_3^2)\}^{1/2}$; $\Delta g = g_1 - g_3$.[14] Cyclic (black) and differential pulse (green) voltammograms (right) in CH_3CN/0.1 M Et_4NClO_4/GC vs SCE (scan rate of 100 mV s^{-1}).

electronic consequence of the ligand backbone[15] as well as its improved redox feature with respect to analogous nacnac.

The quasi-reversible one-electron oxidation and reduction of the isolated complexes (Figure 3 and Figure S8 and Table S10) were assessed by their MO compositions (Tables S11−S26), EPR spectra (Figure 3 and Figure S9), and spin density plots (Figure 4 and Figure S10). It reveals that **2A** or **3A** with the $\{Ru^{III}\text{-}L^-\}$ ($S = {}^1/_2$) configuration undergoes ligand-based oxidation and metal-based reduction to $\{Ru^{III}\text{-}L^{\bullet}\}$ ($S = 0$, $2A^+/3A^+$) and $\{Ru^{II}\text{-}L^-\}$ ($S = 0$, $2A^-/3A^-$), respectively, reemphasizing the RNI of BHM with special reference to the electron releasing process. On the other hand, one-electron oxidation and reduction of Ru(II)-derived **B** or **C** lead to metal (Ru^{II}/Ru^{III})- and ligand (BMO/$BMO^{\bullet-}$ or BAM/$BAM^{\bullet-}$)-based processes, respectively, to which the RNI feature of BMO or BAM can be attributed as well particularly with respect to the electron uptake event (Scheme 3).

Kinetics and Mechanistic Insights of the A → B Transformation. The nonspectator behavior involving methine oxygenation of BHM in **1A**/**2A** was explored in terms of kinetic/thermodynamic and quantum chemical calculations. Oxygenation of **2A** to **2B** was followed spectrophotometrically in deaerated CH_3CN over the temperature range of 303−333 K (Figure 5 and Figure S11 and Table S27), which established a first-order rate with a rate constant (k in s^{-1}) of $(2.9 \pm 0.1) \times 10^{-5}$ at 333 K. The rate of conversion of **2A** to **2B** at varying temperatures extends the kinetic barrier for the process: $\Delta S^{\ddagger}$ (entropy of activation), $\Delta H^{\ddagger}$ (enthalpy of activation), and $\Delta G^{\ddagger}$ (free energy of activation at 298 K) of 4.4 ± 0.1 kcal/mol, −66.4 ± 0.4 cal mol^{-1} K^{-1}, and 24.2 kcal/mol, respectively. The calculated (+)ve $\Delta G^{\ddagger}$ implies the endergonic nature of the intermediate complex formation process as this is associated with the negative entropy of activation (associative pathway). Oxygenation of **1A** also follows similar kinetics but proceeds at a much faster rate [$(7.4 \pm 0.2) \times 10^{-5}$ at 303 K (Figure S12)]. It should be stated that the rate of oxygenation of $\{Ru(acac)_2\}$-coordinated L1 in **1A** is approximately 10 times faster than that of the previously reported[4a] analogous $nacnac^{Ph,Ph}$-derived $[Ru(acac)_2(nacnac^{Ph,Ph})]$ ($k = 6.4 \times 10^{-6}$ s^{-1} at 303 K).

In this scenario, the approach of molecular oxygen ($^3O_2$, $^3\Sigma_g^-$) might have facilitated redox tuning[16] at the metal−ligand interface (Ru^{III}−BHM^- ↔ Ru^{II}−$BHM^{\bullet}$) due to RNI of BHM (*vide infra*). The radical character of BHM in effect favors its interaction with the molecular oxygen (diradical) in a spin-allowed fashion (Scheme 4) to provide transient superoxide radical (I1). Subsequent H shuttling (I2) and cleavage of the O−O bond led to ketonization in **B**.

The enhanced kinetic instability of **1A** over **2A** can be rationalized by its predominant canonical form of Ru^{II}-L1$^{\bullet}$. Ligand-dominated spin facilitates its interaction with $^3O_2$, which is also electronically favored by N atoms at the ring junctions of **1A**. This also justifies the aforementioned much slower rate of oxygenation of $\{Ru(acac)_2\}$-coordinated

Scheme 3. Electronic Structural Forms for the Accessible Redox States of A−C

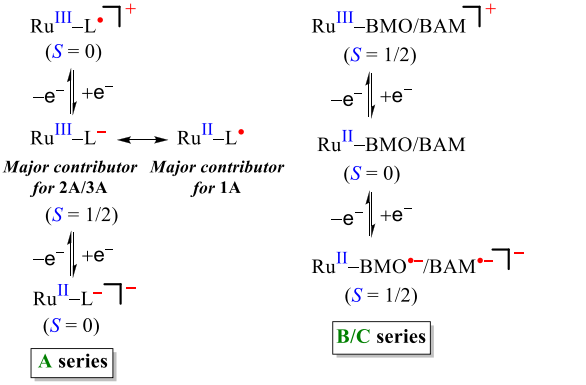

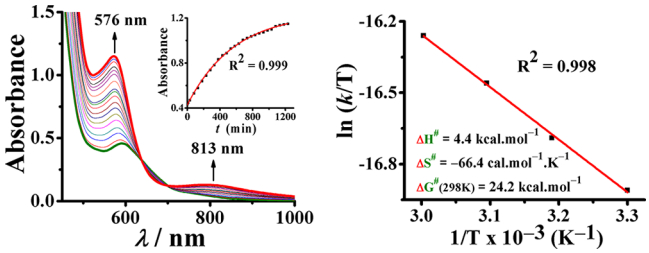

Figure 5. Change in the spectral profile (left) for the **2A** → **2B** conversion at 333 K. The rate is assigned on the basis of the growing feature at 576 nm (inset). Plot of $\ln(k/T)$ vs $1/T$ (right).

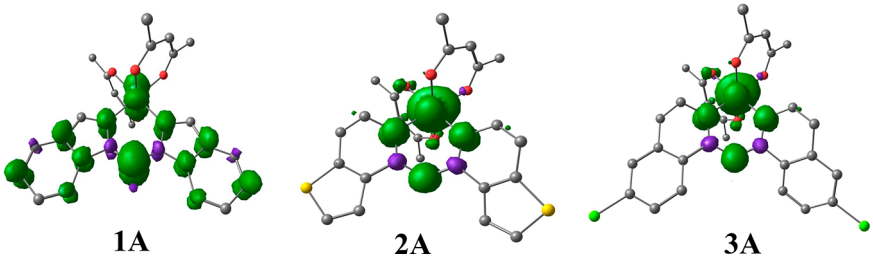

Figure 4. Spin density representations (isosurface value of 0.003).

DOI: 10.1021/acs.inorgchem.9b01201
Inorg. Chem. XXXX, XXX, XXX−XXX

Scheme 4. Aerobic Oxidation Pathway for A → B Conversion

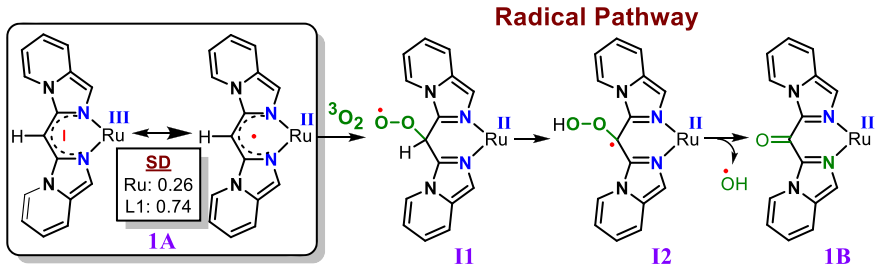

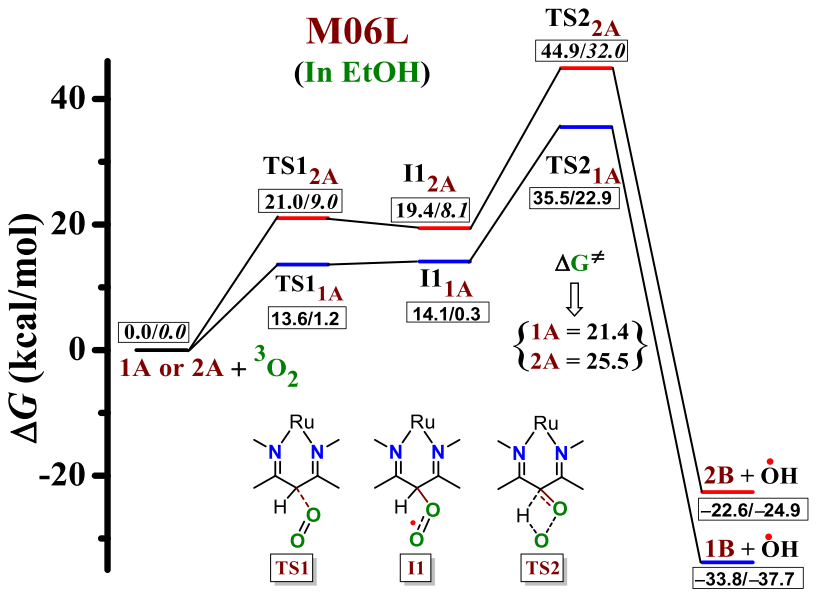

Figure 6. Gibbs free energy (Δ*G*, 298 K) profile of methine oxygenation of Ru-coordinated BHM calculated at the M06L level. The associated Δ*G* and Δ*H* are shown in each state. The Δ*G* of starting substrates is taken as zero. Only core structures are shown here.

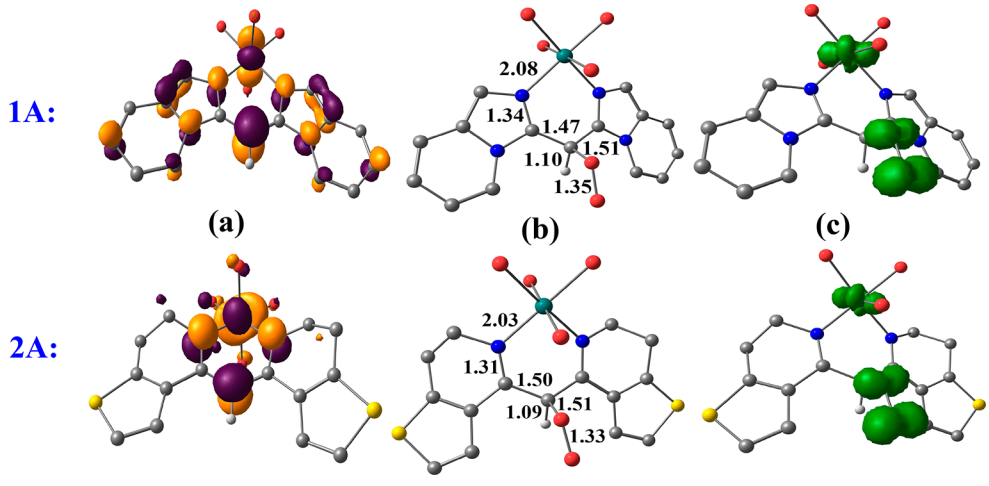

Figure 7. (a) HOMO (isosurface of 0.05) of the reactant, (b) selected bond parameters (computed), and (c) SD plots (isosurface of 0.007) of I1. All H atoms (except C_β-H) and the acac backbone (except O-atoms) have been omitted for the sake of clarity.

nacnac^{Ph,Ph} (SD values of Ru and nacnac of 0.73 and 0.22, respectively)[4a] in comparison to **1A** (SD values of Ru and L1 of 0.26 and 0.74, respectively). This in turn rationalizes the improved reactivity profile of the nacnac analogue (BHM) upon electronic modification. However, we failed to identify the hydroxyl radical, which might be due to its rapid decomposition or participation in other reactions like dehydrogenation of **2B** to **2C** or **3B** to **3C**.

The energy profile diagram [M06L/LANL2DZ/6-31G* in ethanol (Figure 6 and Figure S13)] suggests that metal coordination-promoted interaction of infinitely separated reactants (**1A**/**2A** + $^3O_2$) generates the metastable superoxide intermediate (I1; $S = {}^1/_2$). This proceeds via the formation of a nascent C_β···O bond (TS1) with intrinsic reaction barriers of 13.6 and 21 kcal/mol for **1A** and **2A**, respectively. Concomitant hydrogen transfer from C_β in I1 followed by

DOI: 10.1021/acs.inorgchem.9b01201
Inorg. Chem. XXXX, XXX, XXX−XXX

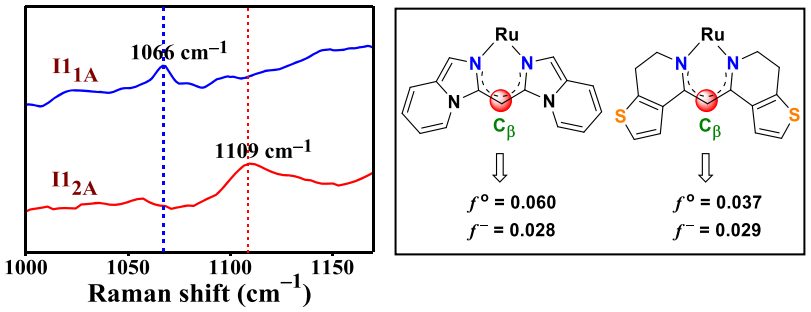

Figure 8. Resonance Raman spectra (left) for the intermediate of **1A** → **1B** (blue) and **2A** → **2B** (red) transformations, detected via time-dependent Raman analysis at 273 K by using a λ_{ex} of 532 nm. Calculated Fukui indices (right) at C_β (f° and f^- stand for radical and nucleophilicity Fukui indices, respectively).

homolytic fission of the O−O bond gives rise to the product (**1B** and **2B**) along with the hydroxyl radical byproduct by overcoming the activation barriers (TS2) of 21.4 and 25.5 kcal/mol for **1A** and **2A**, respectively. The decrease of entropy in the elementary O_2 activation step (**1A** and **2A** to corresponding I1) makes the process endergonic. However, the overall transformation is exergonic due to the improved product stability as a result of incorporation of the carbonyl moiety at the ligand backbone. The lower activation barrier for **1A** → **1B** transformation and the greater thermodynamic stability [free energy of formation (ΔG°)] of **1B** (−33.8 kcal/mol) versus that of **2B** (−22.6 kcal/mol) support the higher oxygenation rate of **1A** as compared to that of **2A**. Moreover, the experimentally deduced activation barrier of **2A** → **2B** conversion ($\Delta G^\ddagger$ of 24.2 kcal/mol, 298 K) correlates well with the calculated value. It is worth noting that the high energy demand for the process makes the **2A** → **2B** conversion kinetically slow at room temperature (>48 h for its completion).

The probable alternate pathway invoving the unfavorable seven-coordinated intermediate of metal-bound O_2, [Ru-(acac)$_2$(BHM)(O_2)], could not be located. The lack of coordination of O_2 to the Ru center also excludes the possibility of the formation of dinuclear Ru−O−O−Ru peroxo species. The involvement of the quartet transition state ($TS1_Q$; $S = {}^3/_2$) (Figure S14) instead of doublet TS1 ($S = {}^1/_2$ in Figure 6) is an energy-demanding process and thus expected to be kinetically unfavorable at room temperature. The use of the UB3LYP functional extends a similar trend (Figure S15).

The selective interaction of π_{1g}*-HOMOs of triplet dioxygen with the C_β center of BHM in **1A** or **2A** to yield the metastable {Ru(BHM-O_2)} intermediate (I1 in Scheme 4) could also be supported by the fact of BHM dominated α-SOMO and β-LUMO (Figure 7a and the Supporting Information). The superoxide form of intermediate I1 (Figure 6) can be conceived by the following considerations: (i) spin localization onto the incoming O2 unit at the ligand backbone (O2, 0.70 and 0.81 for I1 of **1A** and **2A**, respectively) (Figure 7), (ii) estimated O−O bond distance of ∼1.34 Å, (iii) mass spectral profile [m/z 578 for I1 of representative **1A** (Figure S2c)], and (iv) change in the resonance Raman signature as a function of time [experimental and calculated ν_{O-O} 1066 and 1025 cm^{-1} or 1109 and 1099 cm^{-1} for I1 of **1A** or **2A**, respectively (Figure 8)].[17] The decrease in the ν_{O-O} of I1 in **1A** with respect to that in **2A** implies the insertion of a greater extent of peroxide character within the superoxide radical, which also results in a small elongation of the O−O bond.

The slightly elongated C−O bond (∼1.51 Å) in I1 is the reflection of the electronic consequence due to molecular strain.[18] The consideration of radical attack from the nucleophilic methine center (C_β) of BHM in **A** (Scheme 4) has also been justified by the calculation of Fukui indices in which radical Fukui indices are better suited to rationalize the C_β-H functionalization (Figure 8, right).

The enhanced acidity at the pole positions (adjacent to metal-coordinated imine nitrogens) of BMO selectively in **2B** or **3B** facilitates the aerobic dehydrogenation, leading to the formation of thermodynamically stable product **C** in Scheme 2. The conversion of **B** [Ru^{II}(acac)$_2$-coordinated BMO] to **C** [Ru^{II}(acac)$_2$-coordinated BAM] could be rationalized by following the UV−vis spectral changes of the acetonitrile solution of representative **2B** in the presence of excess ^{t}BuOK (Figure 9) under atmospheric conditions. The distinct change

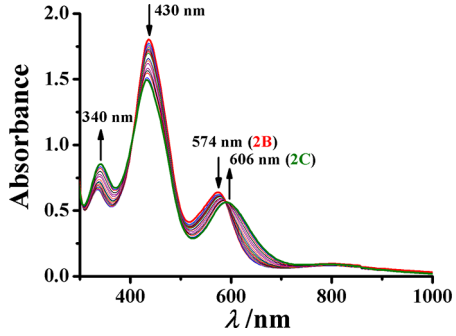

Figure 9. Change in the spectral profile for the **2B** → **2C** conversion in CH_3CN at 298 K in the presence of excess ^{t}BuOK (5 equiv).

in the spectral profile of **2B** (574 → 606 nm) with the isosbestic point at 587 nm in the visible region is consistent with the **2B** → **2C** conversion (see Table 2). The same transformation, however, failed to take place under anoxic conditions (N_2 atmosphere). In addition, upon exposure to air, the **2B** → **2C** conversion also occurred but at a much slower rate (several days). Therefore, it can be considered as a base-promoted oxidative aromatization process of metalated BMO in **B** to afford heteroaromatic substrate BAM in **C**.[9]

CONCLUSION

This work divulges {Ru(acac)$_2$} coordination-assisted oxygenation of nacnac-mimicked BHM in **1A**−**3A** to BMO in **1B**−**3B** and dehydrogenation of resultant ketodiimine-derived BMO to BAM in **2C** and **3C** (Scheme 2). Mechanistic insight reveals the pivotal role of resonance-assisted redox tuning at the

DOI: 10.1021/acs.inorgchem.9b01201
Inorg. Chem. XXXX, XXX, XXX−XXX

metal−ligand interface ($M^pL^n \leftrightarrow M^{p+1}L^{n-1}$) toward the oxygenation of BHM (**A**) to BMO (**B**) (Scheme 2). The superoxide intermediate favoring a radical pathway has been validated through a spectroscopic and transition state theory approach. It also accounts for the improved oxygenation profile of {$Ru(acac)_2$}-coordinated "BHM" with respect to the corresponding "nacnac" derivative as a consequense of electronic modulation at the BHM backbone. The recognition of the pronounced redox non-innocent feature of BHM having a nacnac core may therefore offer additional impetus for multifarious nacnac-based chemistry, including its potential application in the catalytic processes.

EXPERIMENTAL SECTION

Materials. The precursor complex *cis*-[$Ru(acac)_2(CH_3CN)_2$] was prepared by following the literature procedure.[19] EtOH was dried using activated magnesium.[20] Other chemicals and solvents were of reagent grade and used as received. For spectroscopic and electrochemical studies, HPLC grade solvents were used. $^{18}O_2$ was procured from ICON Isotopes.

Physical Measurements. The electrical conductivity was checked using an autoranging conductivity meter (Toshcon Industries). EPR spectra of isolated complexes and electrochemically generated oxidized species were recorded on a Bruker EMX Plus instrument (experimental conditions: microwave frequency of 9.1 GHz with a power of 5 mW and magnetic modulation of 100 kHz with an amplitude of 1 G). Cyclic voltammetric and differential pulse voltammetric measurements of the complexes were performed using a PAR model 273A electrochemistry system. Glassy carbon working, platinum wire auxiliary, and saturated calomel reference electrodes were used in a standard three-electrode configuration with tetraethylammonium perchlorate (TEAP) as the supporting electrolyte (substrate concentration of ≈10^{-3} M; standard scan rate of 100 mV s^{-1}). ^1H and ^{13}C NMR spectra were recorded on Bruker Avance III 400 and 500 MHz spectrometers, respectively. The elemental analyses were performed on a Thermoquest (EA 1112) microanalyzer. Elemental analyses for **1B**, **2C**, and **3C** matched well with the calculated data. However, experimental microanalytical data of **1A**, **2A**, **2B**, **3A**, and **3B** did not match with the corresponding calculated values, presumably due to decomposition. Electrospray mass spectrometry was performed on a Bruker's Maxis Impact (282001.00081) spectrometer. Electronic spectral studies were performed on a PerkinElmer Lambda 1050 spectrophotometer. IR spectra of the complexes as KBr pellets were recorded on a Nicolet spectrophotometer. The Raman spectrum was recorded in a WITec micro-Raman spectrometer equipped with 532 nm Nd:YAG laser excitation.

Kinetic Studies. Kinetic experiments were carried out under an O_2 atmosphere by dissolving **A** (~2×10^{-4} M) in CH_3CN. The change in absorbance at 398 nm for **1A** → **1B** conversion and at 576 nm for **2A** → **2B** conversion was monitored for the rate calculation. The pseudo-first-order rate constant (k) for **A** → **B** conversion was calculated on the basis of a nonlinear exponential fit in Origin Pro8 by following the equation $y = y_0 + A_1 \times \exp(-x/t_1)$, where y and y_0 correspond to the absorbance at 576 nm at time t and time zero, respectively, x corresponds to time periods (t in minutes) over which the absorption changes take place, A_1 is the pseudo-first-order coefficient, and the value of the pseudo-first-order rate constant (k) is $1/(t_1 \times 60)$ s^{-1}.

Crystallography. X-ray diffraction data were collected using a Rigaku Saturn-724+ CCD single-crystal X-ray diffractometer using Mo Kα radiation. The data collection was evaluated by using Crystal Clear-SM Expert. The data were collected by the standard ω-scan technique. The structure was determined by the direct method using SHELXS-97 and refined by full matrix least squares with SHELXL-2014 or SHELXL-2017, refining on F^2.[21] All data were corrected for Lorentz and polarization effects, and all non-hydrogen atoms were refined anisotropically. The remaining hydrogen atoms were placed in geometrically constrained positions and refined with isotropic temperature factors, generally 1.2U_{eq} of their parent atoms. Hydrogen atoms were included in the refinement process as per the riding model. CCDC 1898086 (**HL3**), CCDC 1898087 (**1B**), CCDC 1898089 (**2B**), CCDC 1898090 (**2C**), CCDC 1898091 (**3A**), and CCDC 1898092 (**3C**) contain the supplementary crystallographic data for this paper. These data can be obtained free of charge from The Cambridge Crystallographic Data Centre via www.ccdc.cam.ac.uk/data_request/cif. The alert **B** in the checkCIF of **1B** and **3C** could be ignored as it was developed due to the weakly diffracting nature of the crystals.

Computational Studies. Full geometry optimization was performed by using the density functional theory method at the M06L level.[22] Except for ruthenium, all other elements were assigned the 6-31G* basis set and additional TZVP basis set for representatives **2A**−**2C** to correlate the bond parameters and TD-DFT data. The LANL2DZ basis set with an effective core potential was employed for the ruthenium atom.[23] All calculations were performed with the Gaussian 09 program package.[24] Chemissian 1.7[25] was used to calculate the fractional contributions of various groups to each molecular orbital. Calculated structures were visualized with ChemCraft.[26] Vertical electronic excitations based on M06L-optimized geometries were computed for all using the time-dependent density functional theory (TD-DFT) formalism[27] in acetonitrile using a conductor-like polarizable continuum model (CPCM).[28] Electronic spectra were calculated using SWizard.[29,30]

Transition state calculations were performed at the M06L level of theory starting from infinitely separated substrates. A single imaginary frequency for the transition states (TSs) and real frequencies for local minima were obtained (Table S28). The connectivity of each TS was validated through a relaxed potential energy surface scan for the corresponding reaction coordinate and was found to be the highest-energy point that connected the relevant reactant and product (Figure S16). The zero-point vibrational energies and thermal corrections were obtained from the harmonic frequency calculations at the M06L level of theory (Charts S1 and S2).[22,31] The results obtained using the M06L function has also been tested with the UB3LYP density functional.

Radical Fukui indices (f_A°) and nucleophilicity Fukui indices (f_A^-) were computed[11] with the following equations:

$$f_A^\circ = \{(q_{N+1} - q_{N-1})/2\} \quad \text{(susceptible to radical attack)}$$

$$f_A^- = \{q_N - q_{N-1}\}$$

(susceptible to electrophilic attack/itself acts as a nucleophile)

where q represents the electronic population of atom A in the neutral molecule with N electrons, q_{N+1} represents the electronic population of atom A in the anion with $N + 1$ electrons, and q_{N-1} represents the electronic population of atom A in the cation with $N - 1$ electrons. In this scenario, Fukui function (FF) indices were calculated by using the Hirshfeld population (at the M06L level).

Synthesis of Bis(heterocyclo)methanide Ligands HL1−HL3. Diethyl malonate was added dropwise to the respective amines, and the mixture was vigorously stirred at 100 °C for 48 h to obtain a yellow solid mass corresponding to malonamide derivatives. It was washed with *n*-pentane and dried under vacuum. The malonamide thus obtained was subjected to cyclization by dropwise addition of $POCl_3$ (excess) to a suspension of malonamide and P_2O_5 (excess) in a toluene medium at 0 °C under stirring conditions. After complete addition, the reaction mixture was subjected to reflux overnight. Completion of the reaction was monitored by TLC analysis. A saturated solution of $NaHCO_3$ was added to the ice-cold solution of the aforementioned reaction mixture, until the effervescence ceased. A saturated NaOH solution was then added to adjust the pH to 11. The alkaline solution was extracted using a dichloromethane/H_2O workup and dried over Na_2SO_4. Purification by column chromatography led to the resulting brownish yellow solid of bis(heterocyclo)methanides (**HL**).

DOI: 10.1021/acs.inorgchem.9b01201
Inorg. Chem. XXXX, XXX, XXX−XXX

***HL1**, Bis(imidazo[1,5-a]pyridin-3-yl)methane.* 2-Picolylamine (10.0 mL, 97 mmol), diethyl malonate (7.4 mL, 48.5 mmol). Yield of bis(pyridin-2-ylmethyl)malonamide: 11.9 g (86%). Bis(pyridin-2-ylmethyl)malonamide (10.0 g, 35 mmol), toluene (30 mL), P_2O_5 (50.0 g, 10 equiv), $POCl_3$ (32.9 mL, 10 equiv). Yield of **HL1**: 6.3 g (72%). ^{1}H NMR (400 MHz, $CDCl_3$) δ: 8.11 (d, J = 7.1 Hz, 2H), 7.27 (s, 2H), 7.24 (d, J = 9.3 Hz, 2H), 6.52 (m, 2H), 6.39 (t, J = 6.7 Hz, 2H), 4.78 (s, 2H). ^{13}C NMR (101 MHz, $CDCl_3$) δ: 132.63, 131.07, 121.53, 118.52, 118.44, 118.10, 112.58, 26.98. DEPT-135 (101 MHz, $CDCl_3$) δ: 121.53, 118.52, 118.44, 118.10, 112.58, 26.98. HRMS ($C_{15}H_{12}N_4$) m/z: {**HL1** + H}$^+$ calcd, 249.1135; found, 249.1137.

***HL2**, (Z)-4-[(6,7-Dihydrothieno[3,2-c]pyridin-4(5H)-ylidene)-methyl]-6,7-dihydrothieno[3,2-c]pyridine.* 2-Thiophenethylamine (10.0 mL, 85.4 mmol), diethyl malonate (6.5 mL, 42.7 mmol). Yield of bis(2-thiophenylethyl)malonamide: 12.6 g (92%). Bis(2-thiophenylethyl) malonamide (10.0 g, 31 mmol), toluene (30 mL), P_2O_5 (44.0 g, 10 equiv), $POCl_3$ (29.0 mL, 10 equiv). Yield of **HL2**: 6.2 g (70%). ^{1}H NMR (500 MHz, $CDCl_3$) δ: 11.36 (s, 1H), 7.29 (d, J = 5.1 Hz, 2H), 7.17 (d, J = 5.2 Hz, 2H), 5.57 (s, 1H), 3.81 (t, J = 7.0 Hz, 4H), 3.01 (t, J = 7.0 Hz, 4H). ^{13}C NMR (126 MHz, $CDCl_3$) δ: 153.85, 144.86, 131.40, 124.62, 124.06, 84.43, 40.85, 23.30. DEPT-135 (126 MHz, CDCl3) δ: 124.62, 124.07, 84.43, 40.85, 23.30. HRMS ($C_{15}H_{14}N_2S_2$) m/z: {**HL2** + H}$^+$ calcd, 287.0671; found, 287.0672.

***HL3**, (Z)-6-Chloro-1-[(6-chloro-3,4-dihydroisoquinolin-1(2H)-ylidene)methyl]-3,4-dihydroisoquinoline.* 2-(3-Chlorophenyl)-ethylamine (10.0 mL, 71.9 mmol), diethyl malonate (5.5 mL, 35.4 mM). Yield of bis(3-chlorophenethyl)malonamide: 11.0 g (80%). Bis(3-chlorophenethyl)malonamide (10.0 g, 25.7 mmol), toluene (30 mL), P_2O_5 (36.5 g, 10 equiv), $POCl_3$ (24.0 mL, 10 equiv). Yield of **HL3**: 5.9 g (67%). The dichloromethane solution gave crystals of **HL3**. ^{1}H NMR (500 MHz, $CDCl_3$) δ: 11.52 (s, 1H), 7.72 (d, J = 8.4 Hz, 2H), 7.41−7.30 (m, 3H), 7.26 (s, 2H), 5.88 (s, 1H), 3.68 (t, 4H), 2.88 (t, J = 6.4 Hz, 5H). ^{13}C NMR (126 MHz, $CDCl_3$) δ: 156.92, 138.97, 135.01, 129.76, 127.86, 126.91, 126.02, 84.72, 42.13, 28.29. DEPT-135 (126 MHz, $CDCl_3$) δ: 127.86, 126.91, 126.02, 84.72, 42.13, 28.29. HRMS ($C_{19}H_{16}Cl_2N_2$) m/z: {**HL3** + H}$^+$ calcd, 343.0763; found, 343.0759.

Preparation of Complexes. *Synthesis of [Ru(acac)$_2$(BHM)] (**1A**−**3A**), [Ru(acac)$_2$(BMO)] (**1B**−**3B**), and [Ru(acac)$_2$(BAM)] (**1C**−**3C**).* The complexes were prepared by following the general synthetic routes using respective preformed H-BHM ligands (**HL**) (Scheme S3). To the orange solution of $Ru(acac)_2(CH_3CN)_2$ in degassed EtOH in an oven-dried Schlenk tube were added a yellow solution of the respective BHM derivative in degassed EtOH and Et_3N under a dinitrogen atmosphere. The solution was refluxed under an inert atmosphere for ∼4 h. The solution gradually changed to brownish for **1A** and green for **2A** and **3A**. Evaporation of the solvent under vacuum afforded the solid mass. **A** was sensitive to air and converted to **B** upon exposure to air to different extents based on the substituents in the BHM framework (**3A** ≪ **2A** ≪ **1A**). **1A** was too sensitive to air to be isolated in pure form; thus, only **2A** and **3A** were subjected to purification by column chromatography using neutral alumina and petroleum ether/dichloromethane as the eluent for further study. The removal of solvent under vacuum resulted in corresponding **2A** and **3A**.

To obtain **B** from **A**, the reaction was carried out under an O_2 atmosphere for ∼6 h in an ethanol medium at 373 K. Purification was done by using a neutral alumina column and petroleum ether/dichloromethane.

Though the acidic nature of methylene protons adjacent to imine nitrogens of BMO in **B** led to the aerobic dehydrogenation reaction to yield BAM in **C**, it proceeded at a slower rate. However, addition of a base (e.g., triethylamine or potassium *tert*-butoxide) enhanced the reaction rate. Therefore, heating of **B** in the presence of excess Et_3N in refluxing EtOH resulted in **C**.

*[Ru(acac)$_2$(L1)], **1A** (brown).* $Ru(acac)_2(CH_3CN)_2$ (100 mg, 0.26 mmol), EtOH (50 mL), **HL1** (65.1 mg, 0.26 mmol), Et_3N (0.036 mL, 0.26 mmol). MS (ESI+, CH_3CN) m/z: {**1A** + H}$^+$ calcd, 548.10; found, 548.09.

*[Ru(acac)$_2$(L2)], **2A** (green).* $Ru(acac)_2(CH_3CN)_2$ (100 mg, 0.26 mmol), EtOH (50 mL), **HL2** (75.1 mg, 0.26 mmol), Et_3N (0.036 mL, 0.26 mmol). Yield: 117 mg (76%). MS (ESI+, CH_3CN) m/z: {**2A** + H}$^+$ calcd, 586.05; found, 586.04. Molar conductivity (CH_3CN): Λ_M = 4 Ω^{-1} cm^2 M^{-1}.

*[Ru(acac)$_2$(L3)], **3A** (green).* $Ru(acac)_2(CH_3CN)_2$ (100 mg, 0.26 mmol), EtOH (50 mL), **HL3** (89.8 mg, 0.26 mmol), Et_3N (0.036 mL, 0.26 mmol). Yield: 140 mg (83%). Crystallization was done by slow evaporation of its dichloromethane/hexane (2:1) solution. MS (ESI+, CH_3CN) m/z: {**3A**}$^+$ calcd, 641.05; found, 641.03. Molar conductivity (CH_3CN): Λ_M = 2 Ω^{-1} cm^2 M^{-1}.

*[Ru(acac)$_2$(BMO1)], **1B** (green).* **1A** (50 mg, 0.091 mmol), EtOH (30 mL). Yield: 46 mg (90%). Slow evaporation of its dichloromethane/hexane (2:1) solution gave crystals of **1B**. MS (ESI+, CH_3CN) m/z: {**1B**}$^+$ calcd, 562.08; found, 562.06. ^{1}H NMR (400 MHz, $CDCl_3$) δ: 10.20 (d, J = 7.0 Hz, 2H, CH of the pyridine ring of BMO1), 7.29 (d, J = 8.8 Hz, 2H, CH of the pyridine ring of BMO1), 7.23−7.14 (m, 2H, CH of the pyridine ring of BMO1), 6.58 (t, J = 6.3 Hz, 2H, CH of the pyridine ring of BMO1), 6.16 (s, 2H, CH of the imidazole ring of BMO1), 5.30 (s, 2H, methine CH of acac), 0.98 (s, 6H, CH_3 of acac), 0.71 (s, 6H, CH_3 of acac). ^{13}C NMR (101 MHz, $CDCl_3$) δ: 161.39, 135.78, 130.24, 130.03, 124.30, 123.64, 116.97, 116.11, 53.44, 27.11, 26.95. Anal. Calcd for {**1B**·C_3H_7} $C_{28}H_{31}N_4O_5Ru$: C, 55.60; H, 5.17; N, 9.27. Found: C, 55.25; H, 5.06; N, 8.97. IR (KBr, cm^{-1}): 1628 [ν(C═O)]. Molar conductivity (CH_3CN): Λ_M = 6 Ω^{-1} cm^2 M^{-1}.

*[Ru(acac)$_2$(BMO2)], **2B** (brown).* **2A** (50 mg, 0.085 mmol), EtOH (30 mL). Yield: 44 mg (86%). Slow evaporation of its dichloromethane/hexane (3:1) solution gave crystals of **2B**. MS (ESI+, CH_3CN) m/z: {**2B**}$^+$ calcd, 600.03; found, 600.01. ^{1}H NMR (400 MHz, $CDCl_3$) δ: 7.80 (d, J = 5.0 Hz, 2H, CH of the thiophene ring of BMO2), 7.07 (d, J = 5.2 Hz, 2H, CH of the thiophene ring of BMO2), 5.45 (s, 2H, methine CH of acac), 3.94−3.54 (m, 4H, CH_2 of BMO2), 3.09−2.74 (m, 4H, CH_2 of BMO2), 2.24 (s, 6H, CH_3 of acac), 1.86 (s, 6H, CH_3 of acac). ^{13}C NMR (101 MHz, $CDCl_3$) δ: 188.67, 186.79, 175.50, 140.69, 132.11, 126.37, 121.55, 99.98, 55.53, 27.91, 26.99, 23.25. DEPT-135 (101 MHz, $CDCl_3$) δ: 126.37 (CH of the thiophene ring of BMO2), 121.55 (CH of the thiophene ring of BMO2), 99.98 (CH of acac), 55.53 (CH_2 of BMO2), 27.91 (CH_3 of acac), 26.99 (CH_3 of acac), 23.25 (CH_2 of BMO2). IR (KBr, cm^{-1}): 1712 [ν(C═O)]. Molar conductivity (CH_3CN): Λ_M = 2 Ω^{-1} cm^2 M^{-1}.

*[Ru(acac)$_2$(BMO3)], **3B** (brown).* **3A** (50 mg, 0.078 mmol), EtOH (30 mL). Yield: 31 mg (60%). MS (ESI+, CH_3CN) m/z: {**3B** + H}$^+$ calcd, 657.05; found, 657.05. ^{1}H NMR (400 MHz, $CDCl_3$) δ: 8.14 (s, 2H, CH of BMO3), 7.27 (d, J = 2.1 Hz, 1H, CH of BMO3), 7.25 (d, J = 2.1 Hz, 1H, CH of BMO3), 7.18 (d, J = 1.4 Hz, 2H, CH of BMO3), 5.45 (s, 2H, CH of acac), 3.65 (s, 4H, CH_2 of BMO3), 2.82 (d, J = 39.7 Hz, 4H, CH_2 of BMO3), 2.23 (s, 6H, CH_3 of acac), 1.86 (s, 6H, CH_3 of acac). ^{13}C NMR (101 MHz, $CDCl_3$) δ: 188.86, 186.97, 176.93, 138.65, 134.86, 128.32, 128.00, 127.14, 127.10, 116.33, 100.10, 54.76, 53.43, 27.87, 26.86. DEPT-135 (126 MHz, $CDCl_3$) δ: 128.00 (CH of BMO3), 127.16 (CH of BMO3), 127.11 (CH of BMO3), 100.14 (CH of acac), 54.77 (CH_2 of BMO3), 53.41 (CH_2 of BMO3), 27.90 (CH_3 of acac). IR (KBr, cm^{-1}): 1716 [ν(C═O)]. Molar conductivity (CH_3CN): Λ_M = 6 Ω^{-1} cm^2 M^{-1}.

*[Ru(acac)$_2$(BAM2)], **2C** (green).* **2B** (50 mg, 0.083 mmol), EtOH (30 mL), Et_3N (50 μL, excess). Yield: 35 mg (70%). Slow evaporation of its dichloromethane/hexane (2:1) solution gave crystals of **2C**. MS (ESI+, CH_3CN) m/z: {**2C** }$^+$ calcd, 596.00; found, 595.99. ^{1}H NMR (400 MHz, $CDCl_3$) δ: 8.44 (t, J = 36.4 Hz, 2H, CH of BAM2), 7.83 (s, 2H, CH of BAM2), 7.70 (d, J = 50.7 Hz, 2H, CH of BAM2), 7.09 (d, J = 4.6 Hz, 2H, CH of BAM2), 5.49 (s, 2H, CH of acac), 2.26 (s, 6H, CH_3 of acac), 1.89 (s, 6H, CH_3 of acac). ^{13}C NMR (101 MHz, $CDCl_3$) δ: 186.88, 179.28, 175.54, 140.70, 132.17, 126.41, 121.63, 99.85, 27.98, 23.30. Anal. Calcd for $C_{25}H_{22}N_2O_5S_2Ru$: C, 50.41; H, 3.72; N, 4.70. Found: C, 50.71; H, 3.52; N, 4.74. IR (KBr, cm^{-1}): 1692 [ν(C═O)]. Molar conductivity (CH_3CN): Λ_M = 2 Ω^{-1} cm^2 M^{-1}.

DOI: 10.1021/acs.inorgchem.9b01201
Inorg. Chem. XXXX, XXX, XXX−XXX

*[Ru(acac)$_2$(BAM3)], **3C** (brown).* **3B** (50 mg, 0.076 mmol), EtOH (30 mL), Et_3N (50 μL, excess). Yield: 40 mg (80%). Slow evaporation of its dichloromethane/methanol/hexane (3:1:2) solution gave crystals of **3C**. MS (ESI+, CH_3CN) m/z: $\{\mathbf{3C}\}^+$ calcd, 652.01; found, 652.05. ^{1}H NMR (400 MHz, $CDCl_3$) δ: 9.01 (d, J = 9.2 Hz, 1H, CH of BAM3), 8.81 (d, J = 9.0 Hz, 1H, CH of BAM3), 8.17 (s, 1H, CH of BAM3), 7.80 (d, J = 4.1 Hz, 2H, CH of BAM3), 7.61 (dd, J = 9.2 Hz, 1.7, 3H, CH of BAM3), 7.45 (d, J = 19.6 Hz, 2H, CH of BAM3), 4.98 (s, 1H, CH of acac), 4.61 (s, 1H, CH of acac), 2.02−1.98 (6H, CH_3 of acac), 1.83−1.63 (s, 6H, CH_3 of acac). ^{13}C NMR (101 MHz, $CDCl_3$) δ: 178.61, 147.58, 135.35, 135.30, 129.78, 129.03, 128.95, 127.32, 127.26, 126.31, 125.68, 120.36, 117.43, 28.13, 28.00, 27.80, 25.80. Anal. Calcd for $C_{29}H_{24}N_2O_5Cl_2Ru$: C, 53.38; H, 3.71; N, 4.29. Found: C, 53.18; H, 3.62; N, 4.14. IR (KBr, cm^{-1}): 1702 [ν(C═O)]. Molar conductivity (CH_3CN): Λ_M = 2 Ω^{-1} cm^2 M^{-1}.

■ ASSOCIATED CONTENT

Supporting Information

The Supporting Information is available free of charge on the ACS Publications website at DOI: 10.1021/acs.inorgchem.9b01201.

Bond lengths and angles (crystal and DFT), MO compositions, mass spectra, ^{1}H and ^{13}C NMR spectra, ORTEP diagrams, DFT-optimized structures, kinetic plots, electronic spectra, Gibbs free energy profiles, relaxed potential energy surface plots, and TD-DFT tables (PDF)

Accession Codes

CCDC 1898086−1898087 and 1898089−1898092 contain the supplementary crystallographic data for this paper. These data can be obtained free of charge via www.ccdc.cam.ac.uk/data_request/cif, or by emailing data_request@ccdc.cam.ac.uk, or by contacting The Cambridge Crystallographic Data Centre, 12 Union Road, Cambridge CB2 1EZ, UK; fax: +44 1223 336033.

■ AUTHOR INFORMATION

Corresponding Authors

*E-mail: sanjibp@iitb.ac.in.
*E-mail: lahiri@chem.iitb.ac.in.

ORCID

Achintya Kumar Dutta: 0000-0002-6686-582X
Goutam Kumar Lahiri: 0000-0002-0199-6132

Notes

The authors declare no competing financial interest.

■ ACKNOWLEDGMENTS

Financial support received from the Science and Engineering Research Board (SERB, Department of Science and Technology), a J. C. Bose Fellowship (G.K.L., SERB), CSIR (fellowship to S.P.), and UGC (fellowship to S.K.B.), New Delhi, India, is gratefully acknowledged. The authors thank Prof. D. Maiti, Prof. C. Subramaniam, Mihir Kumar Jha (Department of Chemistry, IIT Bombay), and Vishal Kumar Porwal (Department of Chemistry, IISER Mohali) for their help. The valuable suggestions of the reviewers are also gratefully acknowledged.

■ REFERENCES

(1) (a) Meyer, F.; Tolman, W. B. Forums on Small-Molecule Activation: from Biological Principles to Energy Applications. *Inorg. Chem.* **2015**, *54*, 5039−5039. (b) Yao, S.; Driess, M. Lessons from Isolable Nickel(I) Precursor Complexes for Small Molecule Activation. *Acc. Chem. Res.* **2012**, *45*, 276−287 and references therein . (c) Lyaskovskyy, V.; de Bruin, B. Redox Non-Innocent Ligands: Versatile New Tools to Control Catalytic Reactions. *ACS Catal.* **2012**, *2*, 270−279. (d) Smith, A. L.; Hardcastle, K. I.; Soper, J. D. Redox-Active Ligand-Mediated Oxidative Addition and Reductive Elimination at Square Planar Cobalt(III): Multielectron Reactions for Cross-Coupling. *J. Am. Chem. Soc.* **2010**, *132*, 14358−14360. (e) Suarez, A. I. O.; Lyaskovskyy, V.; Reek, J. N. H.; van der Vlugt, J. I.; de Bruin, B. Complexes with Nitrogen-Centered Radical Ligands: Classification, Spectroscopic Features, Reactivity, and Catalytic Applications. *Angew. Chem., Int. Ed.* **2013**, *52*, 12510−12529. (f) Broere, D. L. J.; Plessius, R.; van der Vlugt, J. I. New Avenues for Ligand-Mediated Processes − Expanding Metal Reactivity by the Use of Redox-Active Catechol, *o*-Aminophenol and *o*-Phenylenediamine Ligands. *Chem. Soc. Rev.* **2015**, *44*, 6886−6915. (g) Cammarota, R. C.; Clouston, L. J.; Lu, C. C. Leveraging Molecular Metal-Support Interactions for H_2 and N_2 Activation. *Coord. Chem. Rev.* **2017**, *334*, 100−111. (h) Ghosh, P.; Dey, S.; Panda, S.; Lahiri, G. K. Solvent-Mediated Functionalization of Benzofuroxan on Electron-Rich Ruthenium Complex Platform. *Chem. - Asian J.* **2018**, *13*, 1582−1593.

(2) (a) Bourget-Merle, L.; Lappert, M. F.; Severn, J. R. The Chemistry of β-Diketiminatometal Complexes. *Chem. Rev.* **2002**, *102*, 3031−3065. (b) Kundu, S.; Phu, P. N.; Ghosh, P.; Kozimor, S. A.; Bertke, J. A.; Stieber, S. C. E.; Warren, T. H. Nitrosyl Linkage Isomers: NO Coupling to N_2O at a Mononuclear Site. *J. Am. Chem. Soc.* **2019**, *141*, 1415−1419. (c) Elwell, C. E.; Gagnon, N. L.; Neisen, B. D.; Dhar, D.; Spaeth, A. D.; Yee, G. M.; Tolman, W. B. Copper−Oxygen Complexes Revisited: Structures, Spectroscopy, and Reactivity. *Chem. Rev.* **2017**, *117*, 2059−2107. (d) MacLeod, K. C.; Menges, F. S.; McWilliams, S. F.; Craig, S. M.; Mercado, B. Q.; Johnson, M. A.; Holland, P. L. Alkali-Controlled C−H Cleavage or N−C Bond Formation by N_2-Derived Iron Nitrides and Imides. *J. Am. Chem. Soc.* **2016**, *138*, 11185−11191. (e) Dai, X.; Kapoor, P.; Warren, T. H. [Me_2NN]Co(η^6-toluene): O═O, N═N, and O═N Bond Cleavage Provides β-Diketiminato Cobalt μ-Oxo and Imido Complexes. *J. Am. Chem. Soc.* **2004**, *126*, 4798−4799. (f) Kundu, S.; Pfaff, F. F.; Miceli, E.; Zaharieva, I.; Herwig, C.; Yao, S.; Farquhar, E. R.; Kuhlmann, U.; Bill, E.; Hildebrandt, P.; Dau, H.; Driess, M.; Limberg, C.; Ray, K. A High-Valent Heterobimetallic [Cu^{III}(μ-$O)_2Ni^{III}]^{2+}$ Core with Nucleophilic Oxo Groups. *Angew. Chem., Int. Ed.* **2013**, *52*, 5622−5626. (g) Company, A.; Yao, S.; Ray, K.; Driess, M. Dioxygenase-Like Reactivity of an Isolable Superoxo−Nickel(II) Complex. *Chem. - Eur. J.* **2010**, *16*, 9669−9675.

(3) (a) Camp, C.; Arnold, J. On the Non-Innocence of "Nacnacs": Ligand-based Reactivity in β-Diketiminate Supported Coordination Compounds. *Dalton Trans.* **2016**, *45*, 14462−14498. (b) Phillips, A. D.; Laurenczy, G.; Scopelliti, R.; Dyson, P. J. Facile, Thermoreversible Cycloaddition of Small Molecules to a Ruthenium(II) Arene β-Diketiminate. *Organometallics* **2007**, *26*, 1120−1122. (c) Radzewich, C. E.; Coles, M. P.; Jordan, R. F. Reversible Ethylene Cycloaddition Reactions of Cationic Aluminum β-Diketiminate Complexes. *J. Am. Chem. Soc.* **1998**, *120*, 9384−9385. (d) Stender, M.; Eichler, B. E.; Hardman, N. J.; Power, P. P.; Prust, J.; Noltemeyer, M.; Roesky, H. W. Synthesis and Characterization of HC{C(Me)N(C_6H_3-2,6-*i*-Pr_2)}$_2MX_2$ (M = Al, X = Cl, I; M = Ga, In, X = Me, Cl, I): Sterically Encumbered β-Diketiminate Group 13 Metal Derivatives. *Inorg. Chem.* **2001**, *40*, 2794−2799. (e) West, N. M.; White, P. S.; Templeton, J. L.; Nixon, J. F. Cycloaddition Reactions of Terminal Alkynes and Phosphaalkynes with an Isolable 5-Coordinate β-Diiminate Platinum(IV) Dihydrosilyl Complex. *Organometallics* **2009**, *28*, 1425−1434.

(4) (a) Panda, S.; Mandal, A.; Ghosh, P.; Lahiri, G. K. Ru-Complex Framework toward Aerobic Oxidative Transformations of β-Diketiminate and α-Ketodiimine. *Inorg. Chem.* **2017**, *56*, 14900−14911 and references therein . (b) Yokota, S.; Tachi, Y.; Itoh, S. Oxidative Degradation of β-Diketiminate Ligand in Copper(II) and Zinc(II) Complexes. *Inorg. Chem.* **2002**, *41*, 1342−1344. (c) Panda, S.; Bera, S. K.; Lahiri, G. K. Electronic Impact of Ancillary Ligand on

DOI: 10.1021/acs.inorgchem.9b01201
Inorg. Chem. XXXX, XXX, XXX−XXX

the Oxygenation Profile of Ruthenium Coordinated β-Diketiminate. *Polyhedron* **2019**, DOI: 10.1016/j.poly.2019.02.052. (d) Scheuermann, M. L.; Fekl, U.; Kaminsky, W.; Goldberg, K. I. Metal-Ligand Cooperativity in O_2 Activation: Observation of a "Pt−O−O−C" Peroxo Intermediate. *Organometallics* **2010**, *29*, 4749−4751. (e) Holze, P.; Corona, T.; Frank, N.; Braun-Cula, B.; Herwig, C.; Company, A.; Limberg, C. Activation of Dioxygen at a Lewis Acidic Nickel(II) Complex: Characterization of a Metastable Organoperoxide Complex. *Angew. Chem., Int. Ed.* **2017**, *56*, 2307−2311.

(5) Fekl, U.; Kaminsky, W.; Goldberg, K. I. A Stable Five-Coordinate Platinum(IV) Alkyl Complex. *J. Am. Chem. Soc.* **2001**, *123*, 6423−6424.

(6) (a) Ghosh, P.; Naastepad, R.; Riemersma, C. F.; Lutz, M.; Moret, M.-E.; Klein Gebbink, R. J. M. Noninnocent β-Diiminate Ligands: Redox Activity of a Bis(alkylimidazole)methane Ligand in Cobalt and Zinc Complexes. *Chem. - Eur. J.* **2017**, *23*, 10732−10737. (b) Khusniyarov, M. M.; Bill, M. M. E.; Weyhermüller, T.; Bothe, E.; Wieghardt, K. Hidden Noninnocence: Theoretical and Experimental Evidence for Redox Activity of a β-Diketiminate(1−) Ligand. *Angew. Chem., Int. Ed.* **2011**, *50*, 1652−1655.

(7) (a) Koehne, I.; Graw, N.; Teuteberg, T.; Herbst-Irmer, R.; Stalke, D. Introducing NacNac-Like Bis(4,6-isopropylbenzoxazol-2-yl)methanide in *s*-Block Metal Coordination. *Inorg. Chem.* **2017**, *56*, 14968−14978. (b) Dauer, D.-R.; Stalke, D. Heterocyclic Substituted Methanides as Promising Alternatives to the Ubiquitous nacnac Ligand. *Dalton Trans.* **2014**, *43*, 14432−14439. (c) Abbotto, A.; Bradamante, S.; Facchetti, A.; Pagani, G. A. Metal Chelation Aptitudes of Bis(*o*-azaheteroaryl)methanes As Tuned by Heterocycle Charge Demands. *J. Org. Chem.* **2002**, *67*, 5753−5772.

(8) (a) Basuli, F.; Huffman, J. C.; Mindiola, D. J. Reactivity at the β-Diketiminate Ligand Nacnac- on Titanium(IV) (Nacnac- = [Ar]NC-(CH_3)CHC(CH_3)N[Ar], Ar = 2,6-$[CH(CH_3)_2]_2C_6H_3$). Diimine-alkoxo and Bis-anilido Ligands Stemming from the Nacnac- Skeleton. *Inorg. Chem.* **2003**, *42*, 8003−8010. (b) Land, M. A.; Huo, B.; Robertson, K. N.; Ylijoki, K. E. O.; Lee, P. T. K.; Areephong, J.; Vidović, D.; Clyburne, J. A. C. Coordination, Reactivity, and Structural Properties of Electron-Rich Ethoxy- and Dimethylamino-Substituted 1,3-Diketiminate Ligands and Their Complexes. *Dalton Trans.* **2018**, *47*, 10195−10205.

(9) (a) Campbell, A. N.; Stahl, S. S. Overcoming the "Oxidant Problem": Strategies to Use O_2 as the Oxidant in Organometallic C-H Oxidation Reactions Catalyzed by Pd (and Cu). *Acc. Chem. Res.* **2012**, *45*, 851−863. (b) Hati, S.; Holzgrabe, U.; Sen, S. Oxidative Dehydrogenation of C-C and C-N Bonds: A Convenient Approach to Access Diverse (Dihydro)heteroaromatic Compounds. *Beilstein J. Org. Chem.* **2017**, *13*, 1670−1692. (c) Zhang, J.; Leitus, G.; Ben-David, Y.; Milstein, D. Facile Conversion of Alcohols into Esters and Dihydrogen Catalyzed by New Ruthenium Complexes. *J. Am. Chem. Soc.* **2005**, *127*, 10840−10841. (d) Saucedo-Vázquez, J. P.; Kroneck, P. M. H.; Sosa-Torres, M. E. The Role of Molecular Oxygen in the Iron(III)- Promoted Oxidative Dehydrogenation of Amines. *Dalton Trans.* **2015**, *44*, 5510−5519.

(10) (a) Yao, Q. J.; Judeh, Z. M. A. 1,1′-Methylene-bis-(1,1′,2,2′,3,3′,4,4′-octahydroisoquinoline): Synthesis, Reaction, Resolution, and Application in Catalytic Enantioselective Transformations. *Tetrahedron* **2011**, *67*, 4086−4092. (b) Bluhm, M. E.; Folli, C.; Pufky, D.; Kroger, M.; Walter, O.; Doring, M. 3-Aminoiminoacrylate, 3-Aminoacrylate, and 3-Amidoiminomalonate Complexes as Catalysts for the Dimerization of Olefins. *Organometallics* **2005**, *24*, 4139−4152.

(11) (a) Ma, Y.; Liang, J.; Zhao, D.; Chen, Y.-L.; Shen, J.; Xiong, B. Condensed Fukui Function Predicts Innate C−H Radical Functionalization Sites on Multi-Nitrogen Containing Fused Arenes. *RSC Adv.* **2014**, *4*, 17262−17264. (b) Korvorapun, K.; Kaplaneris, N.; Rogge, T.; Warratz, S.; Stuckl, A. C.; Ackermann, L. Sequential *meta*-/*ortho*-C−H Functionalizations by One-Pot Ruthenium(II/III) Catalysis. *ACS Catal.* **2018**, *8*, 886−892. (c) Domingo, L. R.; Perez, P.; Saez, J. A. Understanding the Local Reactivity in Polar Organic Reactions Through Electrophilic and Nucleophilic Parr Functions. *RSC Adv.* **2013**, *3*, 1486−1494.

(12) Goswami, V. E.; Walli, A.; Förster, M.; Dechert, S.; Demeshko, S.; Holthausen, M. C.; Meyer, F. Acid/Base Triggered Interconversion of μ-η^2:η^2-Peroxido and Bis(μ-oxido) Dicopper Intermediates Capped by Proton-Responsive Ligands. *Chem. Sci.* **2017**, *8*, 3031−3037.

(13) (a) Kalinina, D.; Dares, C.; Kaluarachchi, H.; Potvin, P. G.; Lever, A. B. P. Spectroscopic, Electrochemical, and Computational Aspects of the Charge Distribution in Ru(acac)$_2$(R-*o*-benzoquinonediimine) Complexes. *Inorg. Chem.* **2008**, *47*, 10110−10126. (b) Rusanova, J.; Rusanov, E.; Gorelsky, S. I.; Christendat, D.; Popescu, R.; Farah, A. A.; Beaulac, R.; Reber, C.; Lever, A. B. P. The Very Covalent Diammino(*o*-benzoquinonediimine) Dichlororuthenium(II) . An Example of Very Strong π-Back-Donation. *Inorg. Chem.* **2006**, *45*, 6246−6262. (c) Ghosh, P.; Banerjee, S.; Lahiri, G. K. Ruthenium Derivatives of in Situ Generated Redox-Active 1,2-Dinitrosobenzene and 2-Nitrosoanilido. Diverse Structural and Electronic Forms. *Inorg. Chem.* **2016**, *55*, 12832−12843. (d) Dey, S.; Panda, S.; Ghosh, P.; Lahiri, G. K. Electronically Triggered Switchable Binding Modes of the *C*-Organonitroso (ArNO) Moiety on the {Ru(acac)$_2$} Platform. *Inorg. Chem.* **2019**, *58*, 1627−1637.

(14) Patra, S.; Sarkar, B.; Mobin, S. M.; Kaim, W.; Lahiri, G. K. Separating Innocence and Non-Innocence of Ligands and Metals in Complexes $[(L)Ru(acac)_2]^n$ (n=−1, 0, + 1; L = *o*-Iminoquinone or *o*-Iminothioquinone). *Inorg. Chem.* **2003**, *42*, 6469−6473.

(15) (a) Mandal, A.; Schwederski, B.; Fiedler, J.; Kaim, W.; Lahiri, G. K. Evidence for Bidirectional Noninnocent Behavior of a Formazanate Ligand in Ruthenium Complexes. *Inorg. Chem.* **2015**, *54*, 8126−8135. (b) Chan, S.-C.; England, J.; Wieghardt, K.; Wong, C.-Y. Trapping of the Putative 1,2-Dinitrosoarene Intermediate of Benzofuroxan Tautomerization by Coordination at Ruthenium and Exploration of its Redox Non-innocence. *Chem. Sci.* **2014**, *5*, 3883−3887. (c) Chakraborty, S.; Laye, R. H.; Paul, R. L.; Gonnade, R. G.; Puranik, V. G.; Ward, M. D.; Lahiri, G. K. A Dinuclear Bis(bipyridine)ruthenium(II) Complex, $[(bpy)_2Ru^{II}\{L^{2-}\}Ru^{II}(bpy)_2]^{2+}$, Incorporating an Unusual Non-innocent Bridging Ligand Containing a *p*-Benzoquinonediimine Fragment: Synthesis, Structure, Redox, and UV/VIS/NIR and EPR Spectroelectrochemical Properties. *J. Chem. Soc., Dalton Trans.* **2002**, 1172−1179. (d) Khan, F. F.; Klein, J.; Priego, J. L.; Sarkar, B.; Jimenez-Aparicio, R.; Lahiri, G. K. Questions of Noninnocence and Ease of Azo Reduction in Diruthenium Frameworks with a 1,8-Bis((*E*)-phenyldiazenyl)-naphthalene-2,7-dioxido Bridge. *Inorg. Chem.* **2018**, *57*, 12800−12810. (e) Butschke, B.; Fillman, K. L.; Bendikov, T.; Shimon, L. J. W.; Diskin-Posner, Y.; Leitus, G.; Gorelsky, S. I.; Neidig, M. L.; Milstein, D. How Innocent are Potentially Redox Non-Innocent Ligands? Electronic Structure and Metal Oxidation States in Iron-PNN Complexes as a Representative Case Study. *Inorg. Chem.* **2015**, *54*, 4909−4926. (f) Bezdek, M. J.; Guo, S.; Chirik, P. J. Terpyridine Molybdenum Dinitrogen Chemistry: Synthesis of Dinitrogen Complexes That Vary by Five Oxidation States. *Inorg. Chem.* **2016**, *55*, 3117−3127.

(16) (a) Straganz, G. D.; Hofer, H.; Steiner, W.; Nidetzky, B. Electronic Substituent Effects on the Cleavage Specificity of a Non-Heme Fe^{2+}-Dependent β-Diketone Dioxygenase and Their Mechanistic Implications. *J. Am. Chem. Soc.* **2004**, *126*, 12202−12203. (b) Steiner, R. A.; Kalk, K. H.; Dijkstra, B. W. Anaerobic Enzyme·Substrate Structures Provide Insight into the Reaction Mechanism of the Copper-Dependent Quercetin 2,3-Dioxygenase. *Proc. Natl. Acad. Sci. U. S. A.* **2002**, *99*, 16625−16630. (c) Khramtsov, V. V.; Bobko, A. A.; Tseytlin, M.; Driesschaert, B. Exchange Phenomena in the Electron Paramagnetic Resonance Spectra of the Nitroxyl and Trityl Radicals: Multifunctional Spectroscopy and Imaging of Local Chemical Microenvironment. *Anal. Chem.* **2017**, *89*, 4758−4771.

(17) (a) Lehnert, N.; Neese, F.; Ho, R. Y. N.; Que, L.; Solomon, E. I. Electronic Structure and Reactivity of Low-Spin Fe(III)−Hydroperoxo Complexes: Comparison to Activated Bleomycin. *J. Am. Chem.*

DOI: 10.1021/acs.inorgchem.9b01201
Inorg. Chem. XXXX, XXX, XXX−XXX

Soc. **2002**, *124*, 10810−10822. (b) Ginsbach, J. W.; Peterson, R. L.; Cowley, R. E.; Karlin, K. D.; Solomon, E. I. Correlation of the Electronic and Geometric Structures in Mononuclear Copper(II) Superoxide Complexes. *Inorg. Chem.* **2013**, *52*, 12872−12874. (c) Bonnot, F.; Tremey, E.; von Stetten, D.; Rat, S.; Duval, S.; Carpentier, P.; Clemancey, M.; Desbois, A.; Niviere, V. Formation of High-Valent Iron-Oxo Species in Superoxide Reductase: Characterization by Resonance Raman Spectroscopy. *Angew. Chem., Int. Ed.* **2014**, *53*, 5926−5930.

(18) Gunbas, G.; Hafezi, N.; Sheppard, W. L.; Olmstead, M. M.; Stoyanova, I. V.; Tham, F. S.; Meyer, M. P.; Mascal, M. Extreme Oxatriquinanes and a Record C-O Bond Length. *Nat. Chem.* **2012**, *4*, 1018−1023.

(19) Kobayashi, T.; Nishina, Y.; Shimizu, K. G.; Satô, G. P. Diacetonitrilebis(*β*-diketonato)Ruthenium(II) Complexes. Their Preparation and Use as Intermediates for the Synthesis of Mixed-Ligand *β*-Diketonato Ruthenium(III) Complexes. *Chem. Lett.* **1988**, *17*, 1137−1140.

(20) Armarego, W. L. F.; Perrin, D. D. *Purification of Laboratory Chemicals*, 4th ed.; Butterworth Heinemann: Oxford, U.K., 1996.

(21) (a) Sheldrick, G. M. A short history of *SHELX*. *Acta Crystallogr., Sect. A: Found. Crystallogr.* **2008**, *A64*, 112−122. (b) Program for Crystal Structure Solution and Refinement; University of Goettingen: Goettingen, Germany, 1997. (c) Sheldrick, G. M. Crystal structure refinement with *SHELXL*. *Acta Crystallogr., Sect. C: Struct. Chem.* **2015**, *71*, 3−8.

(22) Zhao, Y.; Truhlar, D. G. The M06 Suite of Density Functionals for Main Group Thermochemistry, Thermochemical Kinetics, Noncovalent Interactions, Excited States, and Transition Elements: Two New Functionals and Systematic Testing of Four M06-Class Functionals and 12 Other Functionals. *Theor. Chem. Acc.* **2008**, *120*, 215−241.

(23) (a) Andrae, D.; Haeussermann, U.; Dolg, M.; Stoll, H.; Preuss, H. Energy-adjusted *ab initio* Pseudo Potentials for the Second and Third row Transition Elements. *Theor. Chim. Acta* **1990**, *77*, 123−141. (b) Fuentealba, P.; Preuss, H.; Stoll, H.; von Szentpaly, L. A. Proper Account of Core-Polarization with Pseudopotentials: Single Valence-Electron Alkali Compounds. *Chem. Phys. Lett.* **1982**, *89*, 418−422.

(24) Frisch, M. J.; Trucks, G. W.; Schlegel, H. B.; Scuseria, G. E.; Robb, M. A.; Cheeseman, J. R.; Scalmani, G.; Barone, V.; Mennucci, B.; Petersson, G. A.; Nakatsuji, H.; Caricato, M.; Li, X.; Hratchian, H. P.; Izmaylov, A. F.; Bloino, J.; Zheng, G.; Sonnenberg, J. L.; Hada, M.; Ehara, M.; Toyota, K.; Fukuda, R.; Hasegawa, J.; Ishida, M.; Nakajima, T.; Honda, Y.; Kitao, O.; Nakai, H.; Vreven, T.; Montgomery, J. A., Jr.; Peralta, J. E.; Ogliaro, F.; Bearpark, M.; Heyd, J. J.; Brothers, E.; Kudin, K. N.; Staroverov, V. N.; Kobayashi, R.; Normand, J.; Raghavachari, K.; Rendell, A.; Burant, J. C.; Iyengar, S. S.; Tomasi, J.; Cossi, M.; Rega, N.; Millam, J. M.; Klene, M.; Knox, J. E.; Cross, J. B.; Bakken, V.; Adamo, C.; Jaramillo, J.; Gomperts, R.; Stratmann, R. E.; Yazyev, O.; Austin, A. J.; Cammi, R.; Pomelli, C.; Ochterski, J. W.; Martin, R. L.; Morokuma, K.; Zakrzewski, V. G.; Voth, G. A.; Salvador, P.; Dannenberg, J. J.; Dapprich, S.; Daniels, A. D.; Farkas, O.; Foresman, J. B.; Ortiz, J. V.; Cioslowski, J.; Fox, D. J. *Gaussian 09*, revision A.02; Gaussian, Inc.: Wallingford, CT, 2009.

(25) Leonid, S. *Chemissian 1.7*; 2005−2010. Available at http://www.chemissian.com.

(26) Zhurko, D. A.; Zhurko, G. A. *ChemCraft 1.5*; Plimus: San Diego. Available at http://www.chemcraftprog.com.

(27) (a) Bauernschmitt, R.; Ahlrichs, R. Treatment of Electronic Excitations within the Adiabatic Approximation of Time Dependent Density Functional Theory. *Chem. Phys. Lett.* **1996**, *256*, 454−464. (b) Stratmann, R. E.; Scuseria, G. E.; Frisch, M. J. An Efficient Implementation of Time-Dependent Density-Functional Theory for the Calculation of Excitation Energies of Large Molecules. *J. Chem. Phys.* **1998**, *109*, 8218−8225. (c) Casida, M. E.; Jamorski, C.; Casida, K. C.; Salahub, D. R. Molecular Excitation Energies to High-Lying Bound States from Time-Dependent Density Functional Response Theory: Characterization and Correction of the Time-Dependent Local Density Approximation Ionization Threshold. *J. Chem. Phys.* **1998**, *108*, 4439−4450.

(28) (a) Barone, V.; Cossi, M. Quantum Calculation of Molecular Energies and Energy Gradients in Solution by a Conductor Solvent Model. *J. Phys. Chem. A* **1998**, *102*, 1995−2001. (b) Cossi, M.; Barone, V. Time-dependent Density Functional Theory for Molecules in Liquid Solutions. *J. Chem. Phys.* **2001**, *115*, 4708−4718. (c) Cossi, M.; Rega, N.; Scalmani, G.; Barone, V. Energies, Structures, and Electronic Properties of Molecules in Solution with the C-PCM Solvation Model. *J. Comput. Chem.* **2003**, *24*, 669−681.

(29) Gorelsky, S. I. *SWizard*. http://www.sg-chem.net/.

(30) Gorelsky, S. I.; Lever, A. B. P. Electronic Structure and Spectra of Ruthenium Diimine Complexes by Density Functional Theory and INDO/S. Comparison of the Two Methods. *J. Organomet. Chem.* **2001**, *635*, 187−196.

(31) Mondal, B.; Neese, F.; Ye, S. Control in the Rate-Determining Step Provides a Promising Strategy To Develop New Catalysts for CO_2 Hydrogenation: A Local Pair Natural Orbital Coupled Cluster Theory Study. *Inorg. Chem.* **2015**, *54*, 7192−7198.

DOI: 10.1021/acs.inorgchem.9b01201
Inorg. Chem. XXXX, XXX, XXX−XXX